

Article

Vibrational Analysis of a Splash Cymbal by Experimental Measurements and Parametric CAD-FEM Simulations

Spyros Brezas ^{1,*}, Evaggelos Kaselouris ^{1,2}, Yannis Orphanos ^{1,2}, Michael Tatarakis ², Makis Bakarezos ^{1,2},
Nektarios A. Papadogiannis ^{1,2} and Vasilis Dimitriou ^{1,2}

¹ Physical Acoustics and Optoacoustics Laboratory, Hellenic Mediterranean University, Perivolia, 71433 Rethymnon, Greece; vagfem@hmu.gr (E.K.); yorphanos@hmu.gr (Y.O.); bakarezos@hmu.gr (M.B.); npapadogiannis@hmu.gr (N.A.P.); dimvasi@hmu.gr (V.D.)

² Institute of Plasma Physics & Lasers, Hellenic Mediterranean University Centre of Research & Innovation, Tria Monastiria, 74100 Rethymnon, Greece; mictat@hmu.gr

* Correspondence: sbrezas@hmu.gr

Abstract: The present study encompasses a thorough analysis of the vibrations in a splash musical cymbal. The analysis is performed using a hybrid methodology that combines experimental measurements with parametric computer-aided design and finite element method simulations. Experimental measurements, including electronic speckle pattern interferometry, and impulse response measurements are conducted. The interferometric measurements are used as a reference for the evaluation of finite element method modal analysis results. The modal damping ratio is calculated via the impulse response measurements and is adopted by the corresponding simulations. Two different approximations are employed for the computer-aided design and finite element method models: one using three-point arcs and the other using lines to describe the non-smooth curvature introduced during manufacturing finishing procedures. The numerical models employing the latter approximation exhibit better agreement with experimental results. The numerical results demonstrate that the cymbal geometrical characteristics, such as the non-smooth curvature and thickness, greatly affect the vibrational behavior of the percussion instrument. These results are of valuable importance for the development of vibroacoustic numerical models that will accurately simulate the sound synthesis of cymbals.

Keywords: percussion instruments; impact hammer; electronic speckle pattern interferometry; finite element method



Citation: Brezas, S.; Kaselouris, E.; Orphanos, Y.; Tatarakis, M.; Bakarezos, M.; Papadogiannis, N.A.; Dimitriou, V. Vibrational Analysis of a Splash Cymbal by Experimental Measurements and Parametric CAD-FEM Simulations. *Vibration* **2024**, *7*, 146–160. <https://doi.org/10.3390/vibration7010008>

Academic Editors: Sebastian Oberst and Amr M. Baz

Received: 10 November 2023

Revised: 9 January 2024

Accepted: 29 January 2024

Published: 1 February 2024



Copyright: © 2024 by the authors. Licensee MDPI, Basel, Switzerland. This article is an open access article distributed under the terms and conditions of the Creative Commons Attribution (CC BY) license (<https://creativecommons.org/licenses/by/4.0/>).

1. Introduction

Percussion instruments are widely used for creating rhythm in music [1]. Such instruments are the basis for numerous acoustical studies, a summary of which was given by Rossing [2]. A large part of such studies concerns cymbals, which can be played either alone or as part of a drum set. The latter is an assembly of individual percussion instruments, such as bass and snare drums, which primarily emit sound by hitting a membrane under tension. Cymbals also constitute part of a drum set and an individual area of study, due to the complexity of their sound. Cymbals vary in both diameter (from 8 to 30 in) and material. They are usually made of copper-based alloys such as bronze and brass.

The literature [3–16] contains experimental and numerical studies analyzing the vibrational behavior of musical instruments. The normal modes of musical instruments are experimentally measured using a variety of techniques [3], one of which includes the excitation with an impact hammer and the response detection via an accelerometer. The sound is mostly recorded using a single or several microphones [4]. The evolution of holography has provided an additional method for the recording of the vibration modes. Electronic speckle pattern interferometry (ESPI) is a laser-based method, which enables the visualization of the normal modes and the vibration amplitude [5,6]. Finite element

method (FEM) and boundary element method (BEM) analysis are used to numerically investigate the vibrational and acoustic behavior of musical instruments based on their structural characteristics [7–9]. The modeling of musical instruments can be used for the reconstruction of old musical instruments [10] but can also be the basis for sound synthesis of the instruments under investigation [11–13].

Wilbur and Rossing [17] measured more than 100 modes of vibration in a 46 cm diameter crash cymbal using electronic TV holography as the cymbal was driven sinusoidally at an amplitude not leading to nonlinear vibrational behavior, while Fletcher discussed the nonlinearity and the chaotic vibrational behavior in cymbal acoustics [18]. Such nonlinear and chaotic behavior is strongly related to the sound generation by cymbals, as was explicitly presented by Fletcher and Rossing [19]. TV holography was used to visualize such effects [20]. A study in cymbals combining FEM modeling, measurements and holography was performed by Perrin et al. [21]. In continuation of his work, Perrin discussed the non-constant thickness of the cymbal considering varying thickness in the FEM simulations [22]. The variation in thickness and the curvature of the cymbals was the focus point of the detailed theoretical studies of Ducechi et al. [11] and Nguyen et al. [12]; however, the results were not validated by experimental measurements. Recently, Kaselouris et al. [8] performed numerical simulations which included modal and frequency response function finite element analysis, frequency domain and time domain FEM-BEM analysis to study the vibroacoustic behavior of crash and splash cymbals and simulated the motion of a real drumstick for the excitation and vibration of cymbals based on real motion capture data in [7].

In the present research work, an 8 in. cymbal made of MS63 alloy [23] is studied via experimental measurements, such as frequency response function (FRF) techniques using an impact hammer and ESPI, and via FEM FRF and FEM modal analysis. The main scope of this study is to investigate computationally the influence of the cymbal's geometry in its vibrational behavior with reference to the experimental measurements, for vibration amplitudes not leading to nonlinear and chaotic behavior. Therefore, parametric CAD designs of the cymbal are modeled and simulated by FEM. The curved axisymmetric surface profile of the cymbal is computationally designed by two different approximations: (a) by three-point arcs and (b) by lines that may describe the non-smooth curvature of the cymbal, which is introduced from the finishing procedures during manufacturing. In the second approximation, three intervals of sampling points are considered resulting in different CAD geometries. Uniform and varying thickness distributions are considered. The results of the modal analysis for the two approaches, i.e., the computed frequencies of the vibrational modes, are compared in relation to the corresponding ESPI experimental results, which are considered as a reference. The FEM models developed based on the second approximation agree better with the ESPI results due to the modeled non-smooth geometry. FRF FEM simulations are further performed to the CAD-FEM models, whose computed frequencies are at an average difference ratio lower than 5%, compared to the corresponding reference experimental results. In addition to the proposed CAD-FEM simulation approaches, a novel aspect of the current study is the calculation of the modal damping ratio via the FRF experimental measurements and its adoption by the numerical simulations. The FRF computational results are compared with the experimental FRF measurements demonstrating a satisfactory agreement. The numerical results show that the cymbal geometrical characteristics, such as the non-smooth curvature, greatly affect the vibrational behavior of the percussion instrument.

To the authors' knowledge, this is the first time that a detailed CAD-FEM parametric study along with experimental measurements have been used to investigate the vibrational behavior of a cymbal. The upper limit of the frequency range 0–2.5 kHz used in this vibrational study is based on the experimental works of Perrin [21,22] and Wilbur and Rossing [17], which measured the dominant modes of vibration for a crash and a splash cymbal in the linear regime, since the nonlinear and chaotic behavior for higher frequencies

is out of the scope of this work. Herein, the amplitude of the vibrations is lower than the thickness of the cymbal, eliminating the generation of nonlinear vibrations [19].

Furthermore, the findings of this research that highlight the importance of the accurate geometrical characteristics to the vibrational behavior of the instrument hold significant importance in advancing the creation of accurate numerical models for vibroacoustic simulations and synthesizing the sound of cymbals. Such CAD-FEM models are nowadays used in sound emission modeling and simulation studies [7,24,25]. However, achieving a high level of agreement between the recorded and simulated sounds is still challenging, primarily attributed to the intricate nonlinear behavior exhibited by cymbals and the accuracy of the CAD-FEM geometrical parameters.

2. Experimental Measurements

In this section, the experimental procedure, set-ups for the impulse response measurements and the ESPI measurements are described.

2.1. Impulse Response Measurements

A widely used descriptor of a linear system is the FRF, which is the complex ratio between the system output and input. In acoustic measurements, the input of a system is a force, while the output is a quantity related to motion. If the latter is acceleration, the corresponding FRF is termed accelerance. Two estimators are used for measurements, H_1 in case of noise in the output signal and H_2 in case of noise in the input signal. For the presented measurements, the estimator H_2 was used, which is described by

$$H_2(\omega) = \frac{G_{aa}(\omega)}{G_{Fa}(\omega)} \quad (1)$$

where $G_{aa}(\omega)$ is the auto-spectrum of the acceleration and $G_{Fa}(\omega)$ is the cross-spectrum of the force and the acceleration [26].

Figure 1 shows the experimental setup for the FRF measurements. A grid of 144 measurement points is selected on the cymbal (16 radii, along which 9 points are used at 1 cm distance). The cymbal is excited by an impact hammer (Model 086E80, PCB, Depew, NY, USA), and the response is captured by a miniature accelerometer (Model TLD352A56, PCB, Depew, NY, USA), with a mass of ~1.5 g, which is insignificant with respect to the mass of the cymbal. The cymbal is clamped at the hole by a nut, tightened using a torque gauge (Model BTG, Tohnichi, Tokyo, Japan) to secure the clamped boundary conditions. The accelerometer is attached, like a sticker, to a single observation point, commonly hit during playing at the area of the bow, and the excitation is applied at each one of the aforementioned grid points. At each measurement point, an average of ten hammer hits is used for the calculation of the FRF. Following the analysis of another study [27], a similar space-averaged approach for all measurement points was carried out. The recording of the signals and the subsequent analysis is performed by a real-time multi-analyzer (Model OR34, OROS, Inovallée, Meylan, France). For the frequency analysis, the sampling frequency is 51.2 kHz, providing 6401 FFT lines with 3.125 Hz frequency resolution. It must be noted that the signal recorded by the accelerometer can be converted by the multi-analyzer to wav file. This is not the case in relevant studies, where the radiated sound is recorded by microphone at a distance from the cymbal.

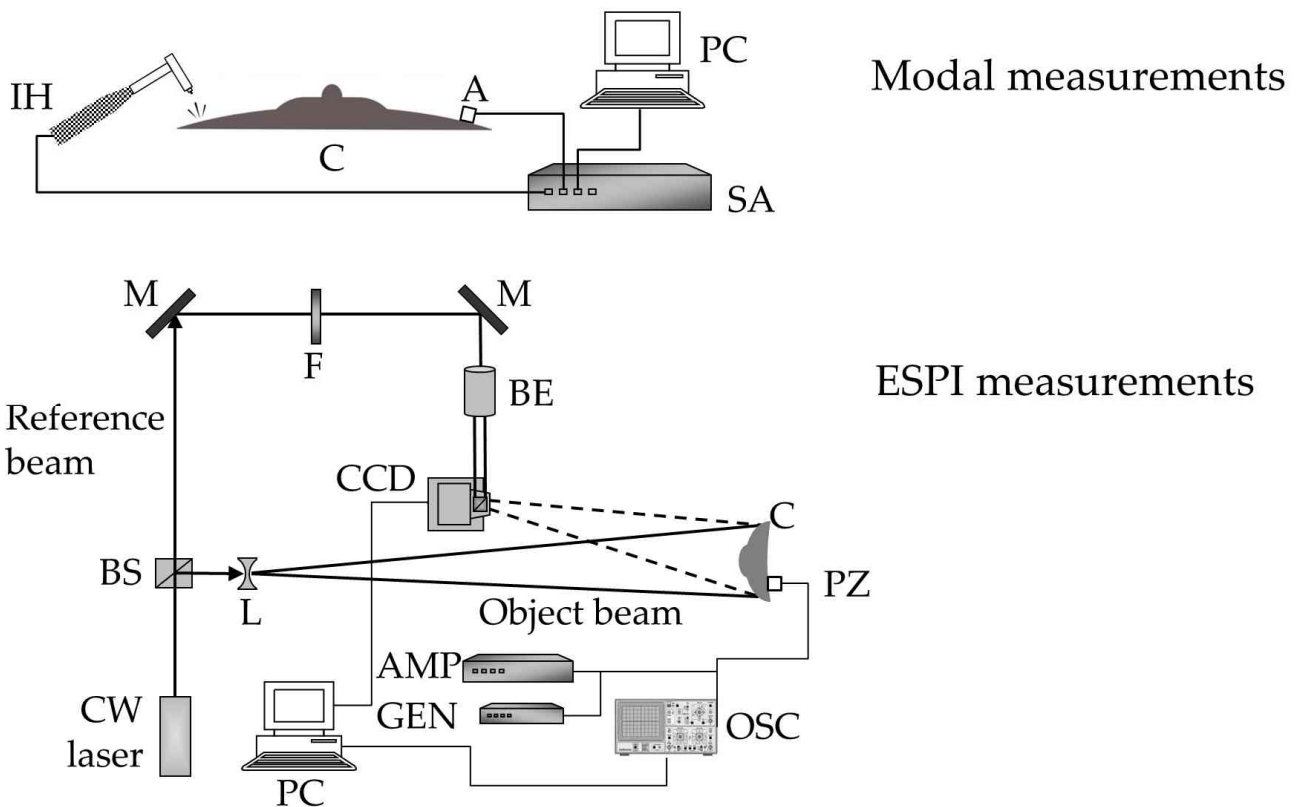


Figure 1. (Top): Experimental setup for the measurement of the frequency response function using an impact hammer (IH) and an accelerometer (A). SA: signal analyzer; C: cymbal; PC: computer with software. (Bottom): Experimental setup for the electronic speckle pattern interferometry measurements. CW laser: 532 nm single longitudinal continuous-wave laser; BS: beam splitter; M: mirror; L: diverging lens; F: variable neutral density filter; BE: beam expander; CCD: camera with beam splitter; C: cymbal; PZ: piezoelectric actuator; GEN: signal generator; AMP: signal amplifier; OSC: oscilloscope; PC: computer with specially developed software.

2.2. Holographic Measurements

The impulse response measurements can determine, among other things, the amplitude and the phase of the indicator used. Therefore, the normal modes can be further analyzed by visualization, which can be implemented using holographic methods [19,28,29]. In the present study, the electronic speckle pattern interferometry (ESPI) [5,6] is used for visualizing the normal modes of the vibrating cymbal.

Figure 1 shows the ESPI experimental setup: the beam of a continuous-wave (CW) single longitudinal mode laser (Model LCX 532, 532 nm, 170 mW, Oxixus, Lannion, France) is split into two parts by means of a cube beam splitter (BS): one part, referred to as the object beam, is used for the illumination of the vibrating cymbal after expansion by a diverging lens (L). The cymbal is vibrated by means of a mini piezoelectric actuator (PZ) controlled by a signal generator (GEN) providing a sinusoidal excitation signal which is appropriately amplified (AMP). The resonances of the modal measurements determine the frequency of the sine signal. An oscilloscope (OSC) is used to accurately monitor and control the PZ input voltage. The intensity of the second beam (reference beam) is controlled by a variable neutral density filter (F) and is expanded by means of a beam expander (BE). The reflected object beam and the reference beam are superimposed on a CCD camera detector with the use of an integrated beam splitter.

A camera captures sequential images of intensity I_1 and I_2 , and the intensity of their subtraction is given by [5].

$$I = I_1 - I_2 = \frac{\sqrt{I_1 I_2}}{2} \left| (\cos \varphi) \Gamma^2 (\Delta A)^2 J_0(\Gamma A) \right| \quad (2)$$

where φ is the phase difference between object and reference beam, $\Gamma = 4\pi/\lambda$, with λ the wavelength of the laser beam, A is the vibration amplitude, ΔA is the vibration amplitude difference between the two images and J_0 is the zero order of the Bessel function of the first kind. The image capturing and the further analysis is performed by specially developed software.

The normal modes occurring at the resonances are shaped by the term $|J_0(\Gamma A)|$. The captured interferogram consists of bright and dark fringes, which are equal height curves with the same vibration amplitude. The bright fringes correspond to the maxima of $|J_0(\Gamma A)|$. Supplementary to the roving hammer results, the ESPI images provide spatial information of the vibrating surface. Additionally, the vibration amplitude, which is perpendicular to the vibrating surface, can be extracted.

3. Mathematical Modeling

FEM is a powerful method that numerically solves differential equations, which concern engineering and multiphysics problems [30–32]. FEM may simulate the vibroacoustic behavior of musical instruments and predicting the reaction of music instruments to different loading conditions, vibrations and variations in the conditions of the environment (such as relative humidity, temperature) [7,8,33]. In this study, modal and FRF analyses are performed via FEM to study the vibrational behavior of the cymbal. LS-DYNA [34] solvers performed the frequency domain modal and FRF FEM analysis and the time domain transient mechanical FEM analysis.

3.1. Mathematical Formulation

The general form of the eigensystem encountered in structural engineering using the FEM is

$$[M] \left\{ \frac{\partial^2 U}{\partial t^2} \right\} + [K] \{U\} = 0 \quad (3)$$

where $[M]$ is the mass matrix, $\{U\}$ is the displacement vector and $[K]$ is the stiffness matrix. FRF is computed using the mode superposition method, in the frequency domain [35]. Assuming that the excitation is applied at node j and the response is evaluated for node k , the acceleration frequency response function F_α may be expressed as:

$$F_\alpha(x_j, x_k, \omega) = -\omega^2 \sum_{n=1}^N \frac{\varphi_n(x_k)}{(-\omega^2 + 2i\zeta_n\omega_n\omega + \omega_n^2)M_n} P_n(x_j) \quad (4)$$

where $P_n(x_j) = \varphi_n^T p(x_j)$, φ_n is the n -th mode shape, $p(x_j)$ is the space distribution of the harmonic force excitation, ω_n are the angular eigenfrequencies and ζ_n is the modal damping ratio [36]. In the case of point force excitation, $p(x_j) = 1$ at node j in specified direction of excitation and 0 elsewhere.

3.2. CAD Modeling

Figure 2b shows a real image of the cymbal geometry studied. The mass weight of the cymbal is 0.380 kg, and the material thickness is assumed to be constant and uniform. The average thickness of the cymbal is ~1.2 mm as measured by a digital caliper. The cymbal radius is 101.6 mm, and its total height is 28 mm. The radius of the flat mounting plateau, including the hole, is 16 mm. The 8'' axisymmetric profile of a cross section of the global geometry is designed on the XZ plane. This profile further revolves about the z-axis cymbal to generate the surface CAD model of the cymbal.

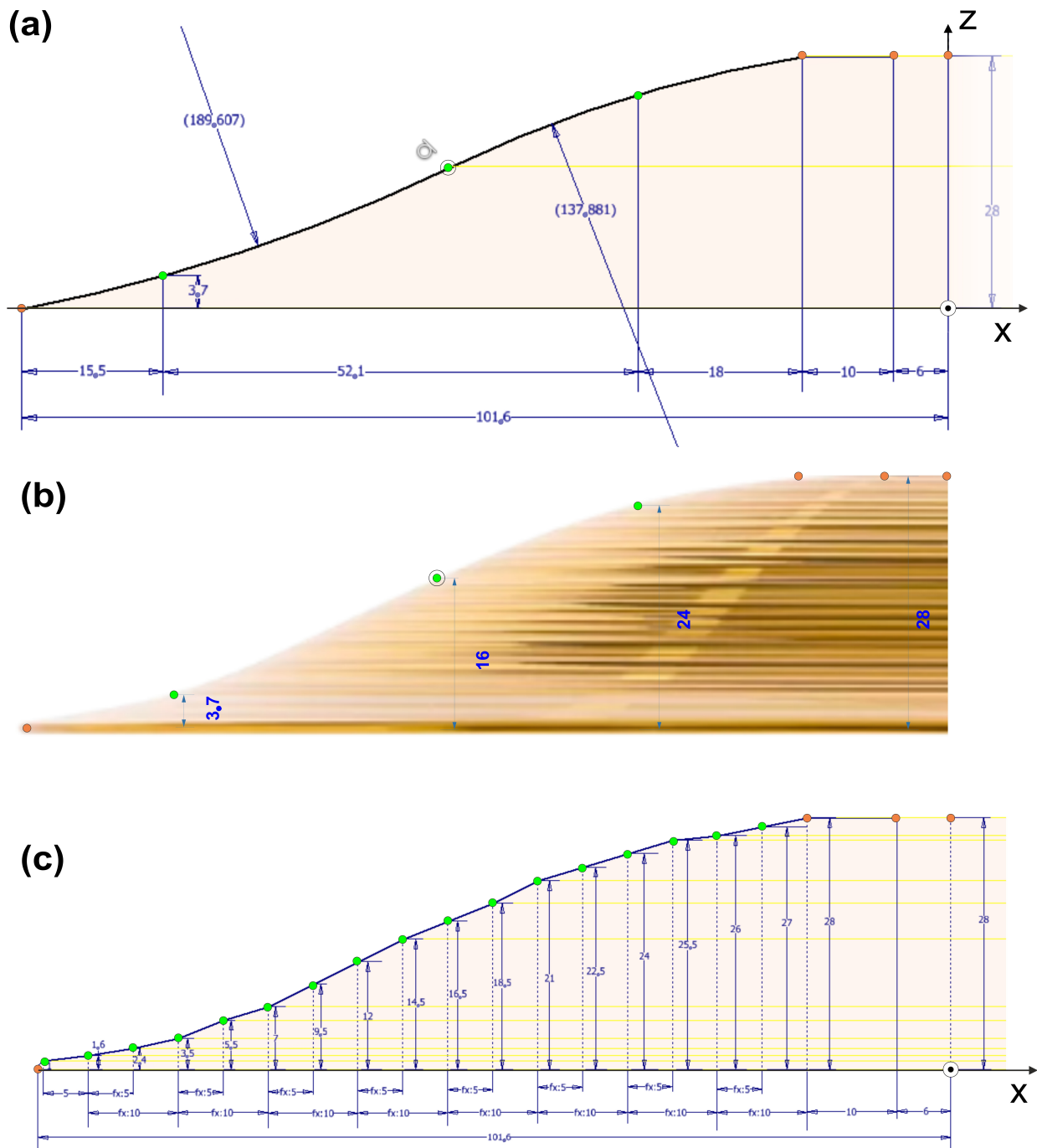


Figure 2. (a) First three-point arc approximation; (b) real image of the splash cymbal; (c) second approximation with lines approximating the non-smooth curvature.

The first modeling approximation is performed by interpolating the bell geometry of the cymbal by arcs. The CAD profile, where the basic construction dimensions are depicted, is presented in Figure 2a. The given predefined dimensions are oriented by orange points, while the curve inflection of the cymbal is indicated at three points, marked green. Based on their spatial position, the curved geometry is interpolated by two three-point arcs. The two arcs, after applying the tangent constrain at their connection point, have a radius of ~190 mm and ~138 mm, as presented in Figure 2a.

The second geometrical modeling approximation is performed by the linear interpolation of points measured on sequential equidistant intervals, using lines, starting at the distance of 16 mm from the symmetry axis Z. Different CAD models are developed

by adopting scanning intervals of 10 mm, 5 mm and 2.5 mm. Figure 2c presents the axisymmetric profile of the cymbal surface derived by using the interval of 5 mm.

3.3. FEM Modeling and Simulation

The revolved surface geometry of the developed profiles is generated and further discretized in the FEM pre-processor LS-Prepost. Approximately 25,000 shell (Belytschko Tsay quadrilateral element) finite elements are generated to model the cymbal. A mesh independent study is performed to provide this number. Regarding the boundary conditions, a clamped constraint is imposed on the nodes bounding the central hole, simulating the cymbal's attachment to a supporting structure [8,20], following the clamped boundary conditions of the experiments. The material properties of MS63 brass alloy used in the simulations can be found in [37]. Two CAD-FEM models are developed for the first approximation using three-point arcs with a constant and uniform thickness of 1.2 mm and 1.3 mm. Additionally, nine CAD-FEM models are developed for the second approximation of lines, which may describe the non-smooth curvature of the cymbal with constant and uniform thicknesses of 1.0 mm, 1.1 mm and 1.2 mm for the three scanning intervals. Furthermore, for the second approximation, two models, with concentrically varying thicknesses, are also considered for the model developed using the scanning interval of 5 mm. The different thicknesses are assigned to the three main parts of the cymbal, the bell, the bow and the edge. The three thickness values for these two cases are (i) 1.3 mm, 1.2 mm and 1.1 mm and (ii) 1.2 mm, 1.1 mm and 1.0 mm, which are assigned to the bell, bow and edge regions, respectively.

FEM modal analysis is carried out, and the simulation results are compared to the experimental ESPI results. FRF FEM simulations are further performed for the three model cases, whose computed frequencies presented a low average difference ratio, compared to the corresponding experimental results. The coordinates of the nodal excitation inputs of the FEM FRF analysis, as well as the nodal response output, are defined according to the experimental measurements. Since the model is axisymmetric, 9 points with 1 cm distance along the radius are excited. The FRF observing point is a single point again, following the experimental measurements. The computed result of the FRF analysis is acceleration, to be directly comparable to the experimental measurements. A resolution of 0.5 Hz is considered for the output frequencies of the FRF analysis, and the modal damping ratio is assumed to be frequency dependent based on our FRF experimental results, which are described in Section 4.

4. Results and Discussion

The block diagram presented in Figure 3 schematically presents the thirteen CAD-FEM models developed for the two CAD approaches. Tables 1–5, denoted over the arrows in the figure, are used for the comparison of the computed resonant frequencies of the FEM simulation modal analysis and the corresponding frequencies experimentally measured by ESPI for the first ten representative modes of vibration which are used as a reference. Measuring the thickness of a cymbal is a challenging task because it typically varies across the edge of the cymbal, and it is not constant from edge to center. A high-precision digital caliper is used to measure the thickness of the cymbal, at the edge and the hole at the bell. The mean thickness is calculated to be ~1.2 mm, as mentioned in Section 3.2, and therefore, the constant and varying thicknesses of 1.0, 1.1 and 1.3 mm are also studied. For each FEM model case, the thickness of the cymbal is given in parenthesis, i.e., for Table 1, FEM (1.2 mm) refers to the FEM model with a thickness of 1.2 mm. Table 1 presents the two model case results of the first CAD approximation, and Tables 2–4 present the results of the nine model cases for the second CAD approximation, for the three intervals, from the coarse scanning of 10 mm (Table 2) to 5 mm (Table 3) and to the density of 2.5 mm (Table 4). Table 5 presents the results for the two model cases with the varying thickness for the second CAD approximation and the scanning interval of 5 mm.

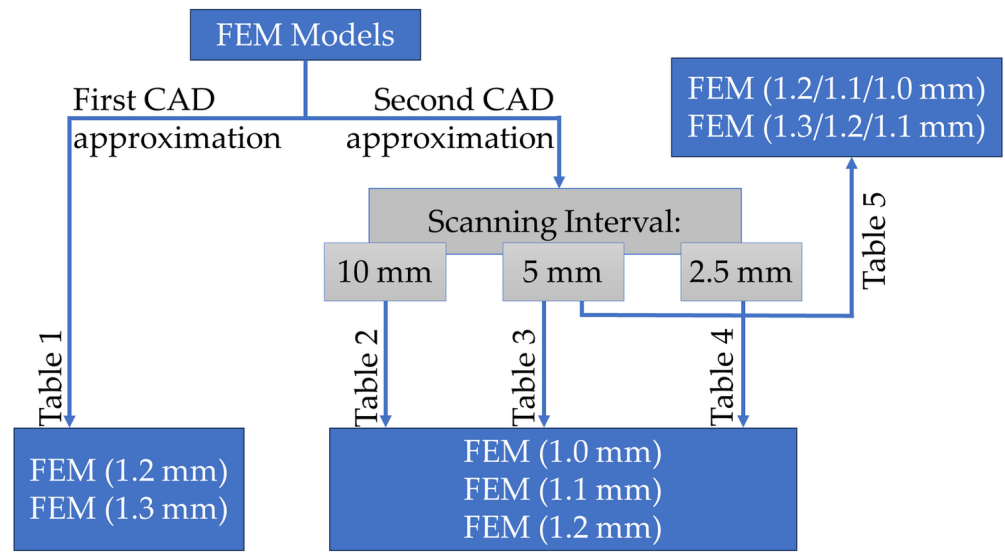


Figure 3. Block diagram of the CAD-FEM models developed and evaluated.

Table 1. FEM results of the first CAD approximation vs. ESPI.

Modes	ESPI (Hz)	FEM (1.2 mm) (Hz)	Difference Ratio%	FEM (1.3 mm) (Hz)	Difference Ratio%
(2,0)	210	215	2.3	225	6.9
(3,0)	555	515	7.5	540	2.7
(4,0)	1040	920	12.2	940	10.1
(5,0)	1520	1200	23.5	1235	20.7
(3,1)	1630	1585	2.8	1655	1.5
(4,1)	1740	1600	8.4	1705	2.0
(2,1)	1760	1855	5.3	1900	7.6
(1,1)	1825	2090	13.5	2130	15.4
(6,0)	1885	1435	27.1	1500	22.7
(5,1)	2030	2010	1.0	2160	6.2
			Average difference ratio%: 10.4		
				Average difference ratio%: 9.6	

Table 2. FEM results of the second CAD approximation (scanning interval 10 mm) vs. ESPI.

Modes	ESPI (Hz)	FEM (1.0 mm) (Hz)	Difference Ratio%	FEM (1.1 mm) (Hz)	Difference Ratio%	FEM (1.2 mm) (Hz)	Difference Ratio%
(2,0)	210	230	9.1	235	11.2	240	13.3
(3,0)	555	585	5.3	605	8.6	625	11.9
(4,0)	1040	1100	5.6	1130	8.3	1150	10.0
(5,0)	1520	1580	3.9	1615	6.1	1650	8.2
(3,1)	1630	1645	0.9	1740	6.5	1830	11.6
(4,1)	1740	1620	7.1	1742	0.1	1860	6.7
(2,1)	1760	1760	0.0	1840	4.4	1920	8.7
(1,1)	1825	1835	0.5	1910	4.5	1975	7.9
(6,0)	1885	1820	3.5	1915	1.6	1990	5.4
(5,1)	2030	1850	9.3	1995	1.7	2145	5.5
			Average difference ratio%: 4.5				
				Average difference ratio%: 5.3		Average difference ratio%: 8.9	

Table 3. FEM results of the second CAD approximation (scanning interval 5 mm) vs. ESPI.

Modes	ESPI (Hz)	FEM (1.0 mm) (Hz)	Difference Ratio%	FEM (1.1 mm) (Hz)	Difference Ratio%	FEM (1.2 mm) (Hz)	Difference Ratio%
(2,0)	210	214	1.9	224	6.4	230	9.1
(3,0)	555	555	0.0	575	3.5	590	6.1
(4,0)	1040	1045	0.5	1075	3.3	1100	5.6
(5,0)	1520	1545	1.6	1575	3.5	1605	5.4
(3,1)	1630	1710	4.8	1800	9.9	1880	14.2
(4,1)	1740	1675	3.8	1795	3.1	1915	9.6
(2,1)	1760	1835	4.2	1915	8.4	1990	12.2
(1,1)	1825	1910	4.6	1980	8.1	2045	11.4
(6,0)	1885	1830	3.0	1910	1.3	1980	4.9
(5,1)	2030	1850	9.3	2010	1.0	2165	6.4
			Average difference ratio%: 3.4			Average difference ratio%: 4.9	Average difference ratio%: 8.5

Table 4. FEM results of the second CAD approximation (scanning interval 2.5 mm) vs. ESPI.

Modes	ESPI (Hz)	FEM (1.0 mm) (Hz)	Difference Ratio%	FEM (1.1 mm) (Hz)	Difference Ratio%	FEM (1.2 mm) (Hz)	Difference Ratio%
(2,0)	210	230	9.1	235	11.2	240	13.3
(3,0)	555	580	4.4	605	8.6	620	11.1
(4,0)	1040	1100	5.6	1120	7.4	1145	9.6
(5,0)	1520	1545	1.6	1585	4.2	1620	6.4
(3,1)	1630	1640	0.6	1735	6.2	1825	11.3
(4,1)	1740	1610	7.8	1730	0.6	1855	6.4
(2,1)	1760	1760	0.0	1840	4.4	1920	8.7
(1,1)	1825	1840	0.8	1910	4.6	1980	8.1
(6,0)	1885	1765	6.6	1860	1.3	1940	2.9
(5,1)	2030	1850	9.3	2000	1.5	2150	5.7
			Average difference ratio%: 4.6			Average difference ratio%: 5.0	Average difference ratio%: 8.4

Table 5. FEM results of the second CAD approximation (varying thickness and for scanning interval 5 mm) vs. ESPI.

Modes	ESPI (Hz)	FEM (1.2/1.1/1.0 mm) (Hz)	Difference Ratio%	FEM (1.3/1.2/1.1 mm) (Hz)	Difference Ratio%	
(2,0)	210	226	7.3	236	11.6	
(3,0)	555	561	1.1	582	4.7	
(4,0)	1040	1056	1.5	1084	4.1	
(5,0)	1520	1553	2.1	1583	4.1	
(3,1)	1630	1715	5.1	1809	10.4	
(4,1)	1740	1683	3.3	1804	3.6	
(2,1)	1760	1838	4.3	1914	8.4	
(1,1)	1825	1910	4.5	1980	8.1	
(6,0)	1885	1835	2.7	1915	1.6	
(5,1)	2030	1866	8.4	2028	0.1	
			Average difference ratio%: 4.0			Average difference ratio%: 5.7

The percentage difference ratio shown in Tables 1–5 is calculated by:

$$\frac{|V_1 - V_2|}{0.5 \times (V_1 + V_2)} \times 100\% \quad (5)$$

where V_1, V_2 are two different values. The modes of vibration are labeled (m,n) , where m describes the number of nodal diameters and n the number of nodal circles.

Based on the results presented in Tables 1–5, the models of the second CAD geometrical approach approximate the experimental results better, if only the average difference ratios are considered. However, the simulation results of the model with a thickness of 1.2 mm using the first CAD approach agree well with the ESPI results, for the first two (2,0) and (3,0) lower frequency modes, while for the (4,0), (5,0), (6,0) modes of the $n = 0$ family, the deviations compared to ESPI increase. The computed results from the second CAD approach for the (4,0), (5,0), (6,0) modes agree better with the ESPI measurements. Furthermore, the results from the three models employing the second CAD approach, with a scanning interval of 5 mm, demonstrate a lower average difference ratio in comparison to the corresponding results from the three models with scanning intervals of 10 mm and 2.5 mm, especially for a uniform thickness equal to 1.0 mm. This gap is particularly evident for modes (2,0), (3,0), (4,0). Also, the model with varying thicknesses of 1.2/1.1/1 mm and a scanning interval of 5 mm results in an average difference ratio of 4.0%. Upon comparing the outcomes of the second approximation for models with uniform thicknesses of 1.0 mm and 1.1 mm and a scanning interval of 5 mm, it becomes evident that the results of the model featuring a uniform thickness of 1.1 mm exhibit a better agreement with the ESPI results for mode (4,1) and for the high-frequency vibrational (6,0) and (5,1) modes; however, the results of the model with a uniform thickness of 1.0 mm demonstrate a better agreement with the ESPI results for all other vibration modes.

Figure 4 demonstrates ten representative modes of vibration, for the FEM cymbal model of the second approximation, with a scanning interval 5 mm and a uniform thickness of 1.0 mm in relation to the ESPI experimental measurements. The modal analysis results agree qualitatively with the results found in the literature [17,21,22] in the linear regime for various cymbal diameters.

Based on the modal results analysis presented, the CAD models developed based on the second CAD approximation, with a scanning interval of 5 mm and a uniform thickness of 1.0 mm and 1.1 mm, as well as the model of varying thicknesses of 1.2/1.1/1.0 mm, are further studied using FRF FEM analysis. For these three models, the average difference ratio, compared to ESPI, is less than 5%. The results of this analysis are compared to the FRF experimental results for the forces of 2.76 N and 34.06 N. The FRF measurement results follow the hammer-accelerometer measurements which are first conducted. The excitation of the cymbal is performed by a handheld hammer hitting the 144 grid points. The average FRF of these 144 excitation points is plotted. The observing point is a single point. During measurements, the variation in the applied mean force (2.76 N and 34.06 N) is used to verify that the linear response of the system remains for the frequency interval considered. It is well known that nonlinear vibrations occur when the amplitude of the vibrations is greater than the thickness of the cymbal [19], which is not the case in our study, since the vibration amplitude for both simulation and experimental results is less than 100 μm . A novel aspect of this study is the experimental measurement of the modal damping ratio, which is equal to $\zeta_n = \frac{\Delta\omega}{2\omega_n}$, where $\Delta\omega$ is the frequency range in which the amplitude of oscillation becomes $A/\sqrt{2}$, with A being the vibration amplitude at the resonance frequency ω_n . Figure 5 demonstrates the experimentally measured modal damping ratio in relation to frequency. These values are adopted by the three models with an average difference ratio of less than 5% vs. ESPI to optimize the numerical approximation.

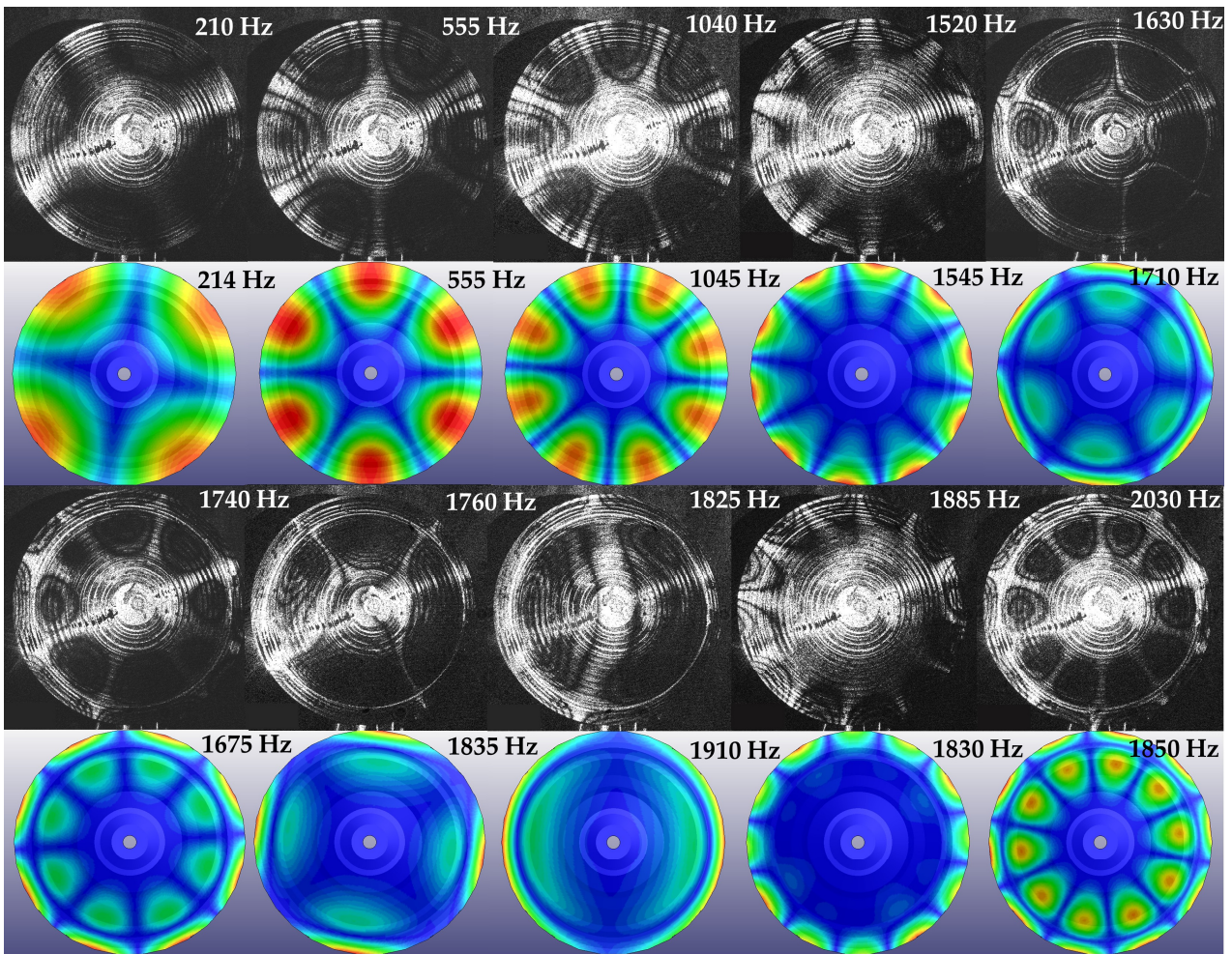


Figure 4. Representative experimental and numerical results of vibrational modes and their corresponding frequencies obtained from the ESPI setup and the FEM simulations, respectively, for the model that presented the lower average difference ratio in relation to ESPI measurements.

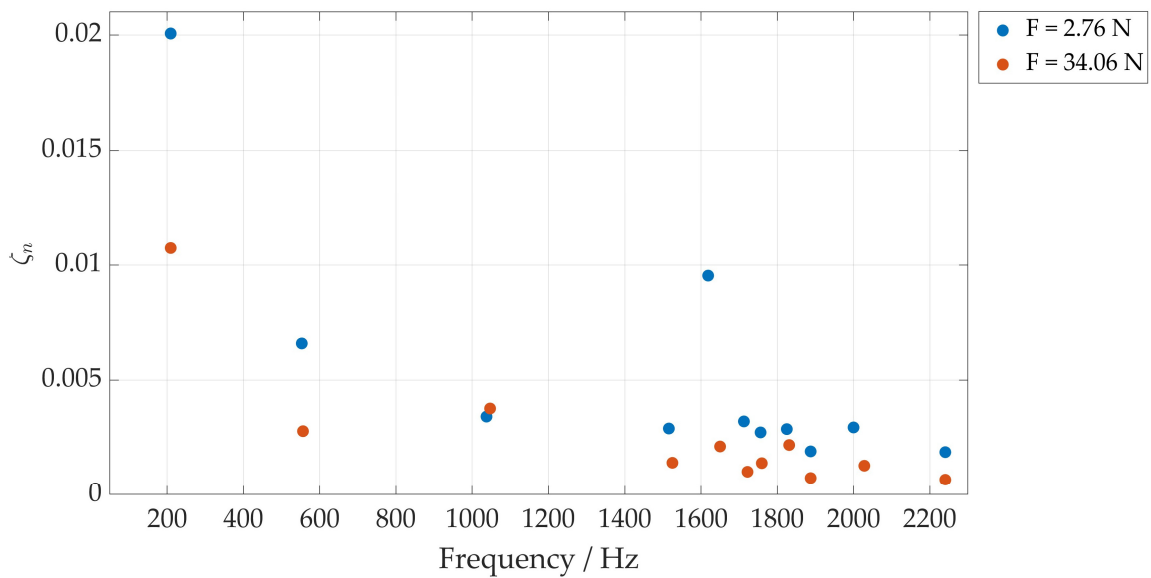


Figure 5. Modal damping ratio in relation to resonance frequencies.

Figures 6 and 7 demonstrate one measurement set for each mean force and the three models for the frequency-dependent modal damping ratio. The graphs in Figures 6 and 7 show the mean acceleration level, presented in descending level order for clarity. Each force value corresponds to a measurement set and is the mean value of the maximum force applied to each measured grid point.

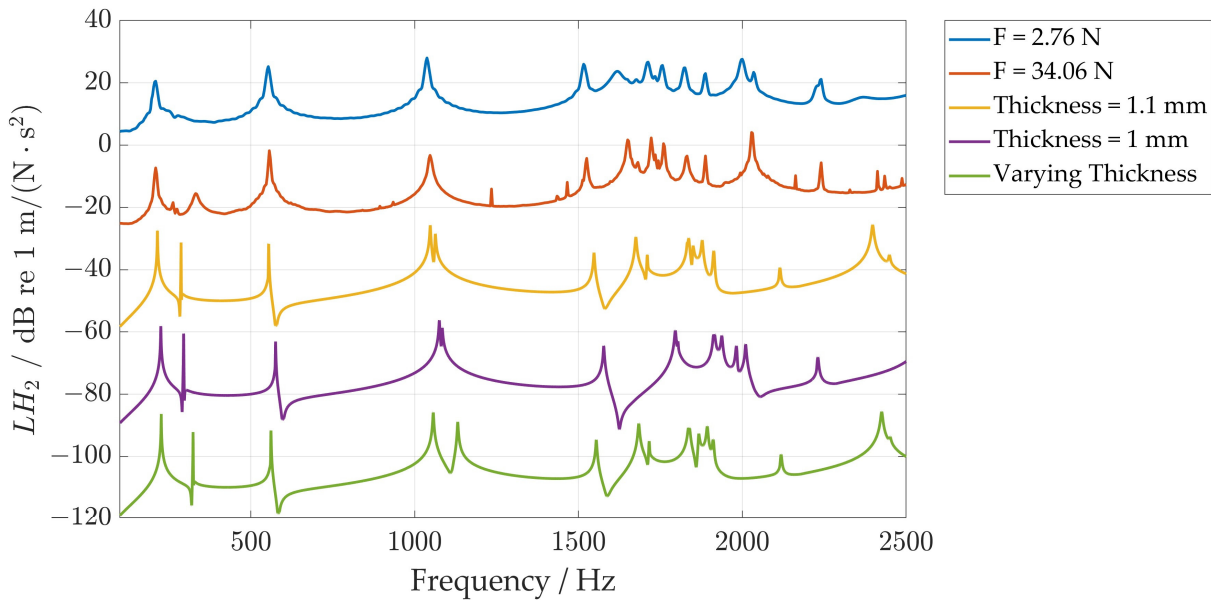


Figure 6. FRF of the measurement set for mean force value (blue line: 2.76 N) and the FEM results of three models with a frequency-dependent modal damping ratio (yellow line: thickness of 1 mm; magenta line: 1.1 mm; green line: varying thicknesses of 1.2/1.1/1.0 mm).

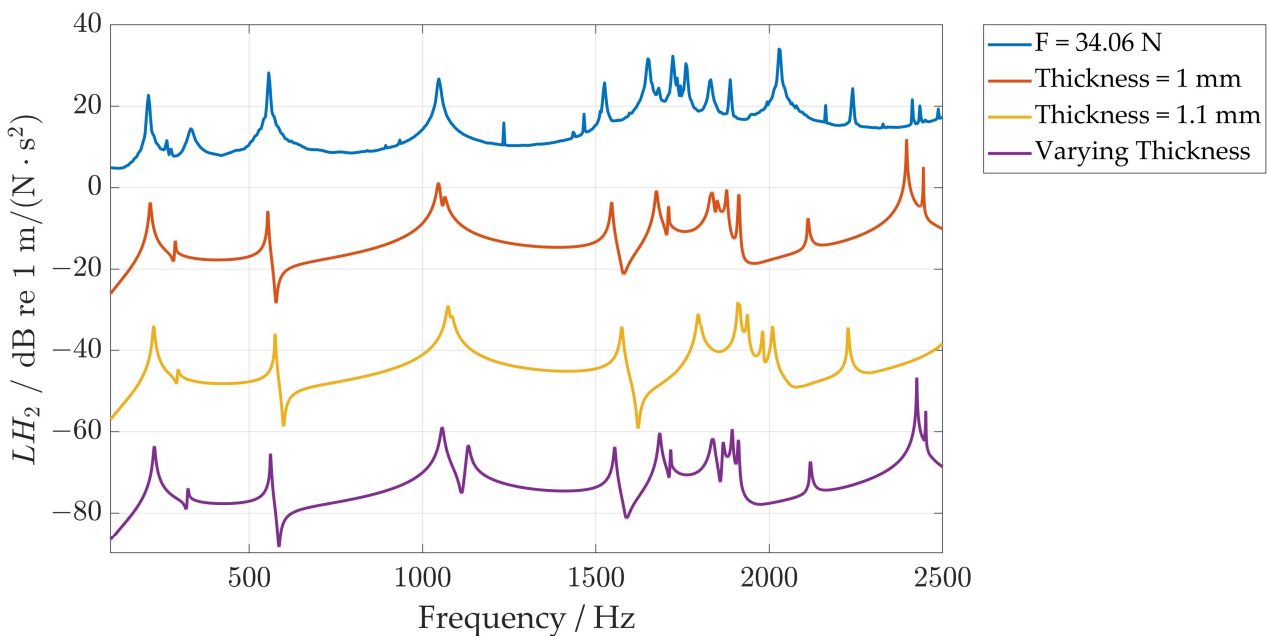


Figure 7. FRF of the measurement set for mean force value (red line: 34.06 N) and the FEM results of three models with a frequency-dependent modal damping ratio (yellow line: thickness of 1 mm; magenta line: 1.1 mm; green line: varying thicknesses of 1.2/1.1/1.0 mm).

The results presented in Figures 6 and 7 demonstrate that the models with frequency-dependent ζ_n provide a good approximation of the FRF experimental results. The simula-

tion results of the model with a thickness of 1.1 mm and the experimental results, presented in Figures 6 and 7, also agree well at ~2250 Hz. This frequency value corresponds to the (7,0) vibration mode, as substantiated by both experimental findings and simulation results. The peak at ~320 Hz corresponds to a bending vibrational mode, as shown by the simulations. Moreover, the model of 1 mm thickness and the one with varying thicknesses provide the vibrational mode observed at ~2400 Hz, which is the (6,1) mode of vibration. Furthermore, the deviations between experimental and numerical results shown in Figures 6 and 7 are mainly attributed to the fact that the CAD-FEM models approximate the geometry of the cymbal well, but slight differences still exist in relation to the real non-smooth and asymmetric micro-geometrical characteristics of the instrument, which are introduced at the finishing of the cymbal during the manufacturing processes.

5. Conclusions

The study delves into a vibrational analysis of a musical splash cymbal using a combination of experimental measurements and parametric CAD-FEM modeling and simulations for vibration amplitudes not leading to nonlinear chaotic behavior. Experimental methods, including impulse response and ESPI measurements, are conducted and validated through FEM FRF analysis and modal analysis, respectively. The CAD-FEM models are developed using two different approximations: three-point arcs and lines, modeling the non-smooth curvature resulting from finishing procedures during manufacturing. Interestingly, the numerical models employing the latter approximation show a better alignment with experimental results. The numerical results demonstrate that the cymbal geometrical characteristics, such as the non-smooth curvature, highly affect the vibrational behavior of the percussion instrument. In addition to the proposed CAD-FEM simulation approaches, a novel aspect of this research study is the calculation of the modal damping ratio via the FRF experimental measurements and its adoption by numerical simulations.

The results of this research study, which highlight the importance of the accurate geometrical characteristics to the vibrational behavior of the instrument, are of valuable importance for the development of vibroacoustic numerical models that will accurately simulate the sound synthesis of cymbals. Such models can aid the generation of lifelike and dynamic cymbal sounds, enabling manufacturers and musicians to experiment with different materials, sizes and performance techniques virtually. Nevertheless, attaining a strong correlation between recorded and simulated cymbal sounds poses a persistent challenge, largely due to the complex nonlinear characteristics inherent in the vibroacoustic behavior of cymbals and the geometrical details of the CAD-FEM models.

Author Contributions: Conceptualization, V.D., E.K., S.B., M.B. and N.A.P.; methodology, S.B., E.K. and Y.O.; software, E.K., S.B. and Y.O.; validation, M.T., M.B. and N.A.P.; investigation, S.B.; writing—original draft preparation, S.B.; writing—review and editing, E.K., M.B. and V.D.; supervision, N.A.P. and V.D. All authors have read and agreed to the published version of the manuscript.

Funding: This research received no external funding.

Data Availability Statement: The data presented in this study are available within the article.

Acknowledgments: This research was funded by the Hellenic Mediterranean University, within the project «Recording and metrological analysis of the vibro-acoustic characteristics of musical instruments for the investigation of alternative and low-cost materials and geometries with relevant sound characteristics». This work was supported with computational time granted by the Greek Research & Technology Network (GRNET) in the National HPC facility ARIS-under project ID pr013024-LaMPIOs II.

Conflicts of Interest: The authors declare no conflicts of interest.

References

1. Scott, E.K.E.; Morrison, A. The acoustics of the modern jazz drum kit. *Acoust. Today* **2022**, *18*, 31–39. [[CrossRef](#)]
2. Rossing, T.D. *Science of Percussion Instruments*, 1st ed.; World Scientific: Singapore, 2000.

3. Duerinck, T.; Segers, J.; Skrodzka, E.; Verberkmoes, G.; Leman, M.; Van Paepegem, W.; Kersemans, M. Experimental comparison of various excitation and acquisition techniques for modal analysis of violins. *Appl. Acoust.* **2022**, *177*, 107942. [CrossRef]
4. Tronchin, L. Structural acoustics of good and bad violins. *J. Acoust. Soc. Am.* **2005**, *117*, 1764–1773.
5. Bakarezos, E.; Orphanos, Y.; Kaselouris, E.; Dimitriou, V.; Tatarakis, M.; Papadogiannis, N.A. Laser-based interferometric techniques for the study of musical instruments. In *Computational Phonogram Archiving*; Springer: Cham, Switzerland, 2019; pp. 251–268.
6. Brezas, S.; Katsipis, M.; Orphanos, Y.; Kaselouris, E.; Kechrakos, K.; Kefaloyannis, N.; Papadaki, H.; Sarantis-Karamesinis, A.; Petrakis, S.; Theodorakis, I.; et al. An Integrated Method for the Vibroacoustic Evaluation of a Carbon Fiber Bouzouki. *Appl. Sci.* **2023**, *13*, 4585. [CrossRef]
7. Kaselouris, E.; Paschalidou, S.; Alexandraki, C.; Dimitriou, V. FEM-BEM Vibroacoustic Simulations of Motion Driven Cymbal-Drumstick Interactions. *Acoustics* **2023**, *5*, 165–176. [CrossRef]
8. Kaselouris, E.; Alexandraki, C.; Bakarezos, M.; Tatarakis, M.; Papadogiannis, N.A.; Dimitriou, V. A detailed FEM Study on the Vibro-acoustic Behaviour of Crash and Splash Musical Cymbals. *Int. J. Circuits Syst. Signal Process.* **2022**, *16*, 948–955. [CrossRef]
9. Chauhan, C.; Singru, P.M.; Vathsan, R. Vibro-acoustic modeling, numerical and experimental study of the resonator and its contribution to the timbre of Sarasvati veena, a South Indian stringed instrument. *J. Acoust. Soc. Am.* **2021**, *149*, 540–555. [CrossRef]
10. Chatziioannou, V. Reconstruction of an early viola da gamba informed by physical modeling. *J. Acoust. Soc. Am.* **2019**, *145*, 3435–3442. [CrossRef]
11. Ducceschi, M.; Touzé, C. Modal approach for nonlinear vibrations of damped impacted plates: Application to sound synthesis of gongs and cymbals. *J. Sound Vib.* **2015**, *344*, 313–331. [CrossRef]
12. Nguyen, Q.B.; Touzé, C. Nonlinear vibrations of thin plates with variable thickness: Application to sound synthesis of cymbals. *J. Acoust. Soc. Am.* **2019**, *145*, 977–988. [CrossRef]
13. Bestle, P.; Eberhard, P.; Hanss, M. Musical instruments–Sound synthesis of virtual idiophones. *J. Sound Vib.* **2017**, *395*, 187–200. [CrossRef]
14. Bretos, J.; Santamaría, C.; Alonso Moral, J. Vibrational patterns of a violin-shaped air cavity obtained by finite element modeling. *Acustica* **1999**, *85*, 584–586.
15. Elejabarrieta, M.J.; Ezcurra, A.; Santamaría, C. Vibrational behaviour of the guitar soundboard analysed by the finite element method. *Acta Acust. United Acust.* **2001**, *87*, 128–136.
16. Lodetti, L.; Gonzalez, S.; Antonacci, F.; Sarti, A. Stiffening Cello Bridges with Design. *Appl. Sci.* **2023**, *13*, 928. [CrossRef]
17. Wilbur, C.; Rossing, T.D. Subharmonic generation in cymbals at large amplitude. *J. Acoust. Soc. Am.* **1997**, *101*, 3144. [CrossRef]
18. Fletcher, N.; Perrin, R.; Legge, K. Nonlinearity and chaos in acoustics. *Acust. Aust.* **1989**, *18*, 9–13.
19. Fletcher, N.; Rossing, T.D. *The Physics of Musical Instruments*; Springer: New York, NY, USA, 1998.
20. Schedin, S.; Gren, P.O.; Rossing, T.D. Transient wave response of a cymbal using double-pulsed TV holography. *J. Acoust. Soc. Am.* **1998**, *103*, 1217–1220. [CrossRef]
21. Perrin, R.; Swallowe, G.M.; Moore, T.R.; Zietlow, S.A. Normal modes of an 18 inch crash cymbal. *Proc. Inst. Acoust.* **2006**, *28*, 653–662.
22. Perrin, R.; Swallowe, G.M.; Zietlow, S.A.; Moore, T.R. The normal model of cymbals. *Proc. Inst. Acoust.* **2008**, *30*, 460–467.
23. Available online: <https://meinlymbals.com/en/products/hcs8b-m3465.html> (accessed on 31 October 2023).
24. Carvalho, M.; Debut, V.; Antunes, J. Physical modelling techniques for the dynamical characterization and sound synthesis of historical bells. *Herit. Sci.* **2021**, *9*, 157.
25. Clinton, J.; Wani, K. Extracting Vibration Characteristics and Performing Sound Synthesis of Acoustic Guitar to Analyze Inharmonicity. *Open J. Acoust.* **2020**, *10*, 41–50. [CrossRef]
26. Mc Connell, K.G.; Varoto, P.S. *Vibration Testing: Theory and Practice*; John Wiley & Sons: New York, NY, USA, 2008.
27. Tronchin, L. Modal analysis and intensity of acoustic radiation of the kettledrum. *J. Acoust. Soc. Am.* **2005**, *117*, 926–933. [CrossRef]
28. Bader, R.; Fischer, J.; Münster, M.; Kontopidis, P. Metamaterials in musical acoustics: A modified frame drum. *J. Acoust. Soc. Am.* **2019**, *145*, 3086–3094. [CrossRef]
29. Ishikawa, K.; Yatabe, K.; Oikawa, Y. Seeing the sound of castanets: Acoustic resonances between shells captured by high-speed optical visualization with 1-mm resolution. *J. Acoust. Soc. Am.* **2020**, *148*, 3171–3180. [CrossRef]
30. Zienkiewicz, O.C. *The Finite Element Method in Engineering Science*; McGraw-Hill: New York, NY, USA, 1971.
31. Zienkiewicz, O.C.; Taylor, R.L.; Zhu, J.Z. *The Finite Element Method: Its Basis and Fundamentals*, 7th ed.; Butterworth-Heinemann: Oxford, UK, 2013.
32. Kaselouris, E.; Nikolos, I.K.; Orphanos, Y.; Bakarezos, M.; Papadogiannis, N.A.; Tatarakis, M.; Dimitriou, V. Elastoplastic study of nanosecond-pulsed laser interaction with metallic films using 3D multiphysics fem modeling. *Int. J. Damage Mech.* **2016**, *25*, 42–55. [CrossRef]
33. Kaselouris, E.; Bakarezos, M.; Tatarakis, M.; Papadogiannis, N.A.; Dimitriou, V. A Review of Finite Element Studies in String Musical Instruments. *Acoustics* **2022**, *4*, 183–202. [CrossRef]
34. Hallquist, J.O. *LS-DYNA Theory Manual*; Livermore Software Technology Corporation: Livermore, CA, USA, 2006.
35. Frequency domain. In *LS-DYNA Theory Manual*; Livermore Software Technology Corporation: Livermore, CA, USA, 2023; Chapter 47; pp. 855–857.

-
36. Ewins, D.J. *Modal Testing: Theory, Practice and Application (Mechanical Engineering Research Studies: Engineering Dynamics Series)*, 2nd ed.; Wiley: Hoboken, NJ, USA, 2009.
 37. Available online: <https://barneelloyd.files.wordpress.com/2013/03/barnee-lloyd-frequency-analysis-of-a-cymbal-paper-incl-all-references.pdf> (accessed on 31 October 2023).

Disclaimer/Publisher's Note: The statements, opinions and data contained in all publications are solely those of the individual author(s) and contributor(s) and not of MDPI and/or the editor(s). MDPI and/or the editor(s) disclaim responsibility for any injury to people or property resulting from any ideas, methods, instructions or products referred to in the content.